JOURNAL OF GEOPHYSICAL RESEARCH, VOL. 115, A04202, doi:10.1029/2008JA014023, 2010

Use of POES SEM-2 observations to examine radiation belt dynamics and energetic electron precipitation into the atmosphere

Craig J. Rodger,[1] Mark A. Clilverd,[2] Janet C. Green,[3] and Mai Mai Lam[2]

Received 26 December 2008; revised 2 August 2009; accepted 3 November 2009; published 3 April 2010.

[1] The coupling of the Van Allen radiation belts to the Earth's atmosphere through precipitating particles is an area of intense scientific interest. Currently, there are significant uncertainties surrounding the precipitating characteristics of medium energy electrons (>20 keV), and even more uncertainties for relativistic electrons. In this paper we examine roughly 10 years of measurements of trapped and precipitating electrons available from the Polar Orbiting Environmental Satellites (POES)/Space Environment Monitor (SEM-2), which has provided long-term global data in this energy range. We show that the POES SEM-2 detectors suffer from some contamination issues that complicate the understanding of the measurements, but that the observations provide insight into the precipitation of energetic electrons from the radiation belts, and may be developed into a useful climatology for medium energy electrons. Electron contamination also allows POES/SEM-2 to provide unintended observations of >700 keV relativistic electrons. Finally, there is an energy-dependent time delay observed in the POES/SEM-2 observations, with the relativistic electron enhancement (electrons >800 keV) delayed by approximately one week relative to the >30 keV electron enhancement, probably due to the timescales of the acceleration processes. Observations of trapped relativistic electron fluxes near the geomagnetic equator by GOES show similar delays, indicating a "coherency" to the radiation belts at high and low orbits, and also a strong link between trapped and precipitating particle fluxes. Such large delays should have consequences for the timing of the atmospheric impact of geomagnetic storms.

Citation: Rodger, C. J., M. A. Clilverd, J. C. Green, and M. M. Lam (2010), Use of POES SEM-2 observations to examine radiation belt dynamics and energetic electron precipitation into the atmosphere, *J. Geophys. Res.*, *115*, A04202, doi:10.1029/2008JA014023.

1. Introduction

[2] The coupling of the Van Allen radiation belts to the Earth's atmosphere through precipitating particles is an area of intense scientific interest, principally due to two differing research activities. One of these concerns the physics of the radiation belts, and primarily the evolution of energetic electron fluxes during and after geomagnetic storms [e.g., *Reeves et al.*, 2003]. The other focuses on the response of the atmosphere to precipitating particles, with a possible linkage to climate variability [e.g., *Turunen et al.*, 2009]. Both scientific areas require increased understanding of the nature of the precipitation, particularly as to the precipitation drivers, as well as the variation of the flux and energy spectrum for electrons lost from the outer radiation belts.

[3] Essentially all geomagnetic storms substantially alter the electron radiation belt populations, reflecting acceleration, loss, and transport processes [*Reeves et al.*, 2003, 2009], in which precipitation losses into the atmosphere play a major role [*Green et al.*, 2004]. A significant fraction of all of the particles lost are precipitated into the atmosphere [*Lorentzen et al.*, 2001; *Horne*, 2002; *Friedel et al.*, 2002; *Clilverd et al.*, 2006], although storm-time nonadiabatic magnetic field changes also lead to losses through magnetopause shadowing [e.g., *Ukhorskiy et al.*, 2006]. The geomagnetic activity which drives the radiation belt variability [*Friedel et al.*, 2002] may come from either high-speed solar wind-streams (HSSWS) in the solar wind or the arrival of interplanetary coronal mass ejections (ICMEs). While ICMEs are the main source of geomagnetic storms at solar maximum, the declining and minimum phase of the 11-year solar activity cycle is characterized by an increase in the occurrence rate of high-speed (>500 km/s) solar wind-streams emanating from coronal holes [*Richardson et al.*, 2000].

[4] Recently there has been much interest in the varying responses of the radiation belt to HSSWS and ICMEs [*Borovsky and Denton*, 2006]. Although HSSWS events are not typically associated with large signatures in the D_{st} index (min > −50 nT), they do produce moderate levels of

[1]Department of Physics, University of Otago, Dunedin, New Zealand.
[2]Physical Sciences Division, British Antarctic Survey, Cambridge, UK.
[3]Space Weather Prediction Center, NOAA, Boulder, Colorado, USA.

0148-0227/10/2008JA014023

Table 1. Detectors That Are Part of the POES Space Environment Monitor-2 (SEM-2) Package Used in the Current Study[a]

Data Channel	Energy Passband	Directionality	Contaminant
e1	>30 keV	0°, 90°	210–2700 keV protons
e2	>100 keV	0°, 90°	280–2700 keV protons
e3	>300 keV	0°, 90°	440–2700 keV protons
P1	30–80 keV	0°, 90°	none
P2	80–240 keV	0°, 90°	none
P3	240–800 keV	0°, 90°	none
P6	>6.9 MeV	0°, 90°	electrons above 700 keV
$P6_{omni}$	>16 MeV	0°	electrons above 800 keV
$P7_{omni}$	>36 MeV	0°	none

[a]The telescopes viewing 0° and 90° are ±15° wide, while the omnidirectional detectors (labeled "omni") are ±60° wide. The nature of the relativistic electron contamination for the P6 and $P6_{omni}$ detectors is described in section 4.

geomagnetic activity that persist for many days. In contrast, ICME events are more transient, driving high geomagnetic activity for typically only 1–2 days [*Richardson et al.*, 2000]. As such, the energy input to the magnetosphere during HSSWS events is believed to be comparable to or to exceed the energy input to the magnetosphere during ICMEs. It has been suggested that there are more long-lasting radiation belt electron flux enhancements in HSSWS-driven storms compared to ICME-driven storms [*Miyoshi and Kataoka*, 2005], that the flux of higher-energy particles peak later in time, and that many magnetospheric electromagnetic wave processes are enhanced [*Hilmer et al.*, 2000; *Vassiliadis et al.*, 2007].

[5] The impact of precipitating particles on the environment of the Earth is also an area of current scientific focus. Precipitating charged particles produce odd nitrogen NO_x ($NO + NO_2$) in the Earth's atmosphere, which can catalytically destroy ozone [*Brasseur and Solomon*, 2005]. As a result, energetic particle precipitation (EPP) events have been linked to significant decreases in polar ozone in the upper stratosphere [e.g., *Randall et al.*, 2005]. Multiple observations undertaken during the Arctic winter of 2003–2004 showed two periods of EPP-linked polar ozone loss at ~40 km altitude, with decreases of ~30% and ~17% [*Seppälä et al.*, 2007]. By influencing stratospheric ozone variability, EPP can affect the stratospheric radiative balance and may link to climate variability. *Rozanov et al.* [2005] imposed a NO_x source calculated from 1987 NOAA TIROS spacecraft EEP measurements to represent this linkage into their chemistry-climate model and found large (±2 K) variations in polar surface air temperatures. They concluded that the magnitude of the atmospheric response to EEP events can potentially exceed the effects from solar UV fluxes. Very recently, the pattern and magnitude of the polar surface air temperature-variability predicted by *Rozanov et al.* [2005] has been observed in European Centre for Medium-Range Weather Forecast ERA-40 reanalysis data, with the surface air temperature-variability associated with geomagnetic disturbances being roughly twice that associated with solar cycle UV variability [*Seppälä et al.*, 2009].

[6] Few ground-based data sets have the combination of long time series and near-global spatial coverage to describe the variation in precipitation into the atmosphere. For example, the AARDDVARK array of subionospheric radio receivers [*Clilverd et al.*, 2009] and the GLORIA riometer array [*Alfonsi et al.*, 2008] are examples of relevant, but currently limited, ground-based instruments. There are also few spacecraft measurements available that measure precipitating electron fluxes and energy spectra in the bounce loss cone for the energy range >20 keV and which have flown for sufficiently long time periods. One spacecraft instrument that has provided long-term global data is the Space Environment Monitor (SEM-2) instrument package onboard the Polar Orbiting Environmental Satellites (POES). In this paper we examine roughly 10 years of measurements of trapped and precipitating electrons available from POES. This data set includes both medium and relativistic energy-range measurements of trapped and precipitating electrons, from the same spacecraft. While the detectors suffer from some contamination issues that complicate the understanding of the measurements, we show that the POES/SEM-2 observations provide additional insight into the precipitation of energetic electrons from the radiation belts and may be developed into a useful climatology. While many radiation belt processes take place around the geomagnetic equator and are best studied by instruments that pass near this location, studies into the loss of particles from the radiation belt through atmospheric are best examined by instruments near the feet of the field lines. The low altitudes of the POES platforms make them well suited for viewing particles near or in the loss cone and hence allow a focus on the timescale of processes that drive particles into the atmosphere.

2. POES Particle Instrumentation

[7] In this study we make use of particle measurements by the SEM-2 instrument package onboard the POES spacecraft, which are in Sun-synchronous orbits at ~800–850 km altitudes. SEM-2 includes the Medium Energy Proton and Electron Detector (MEPED) in addition to the Total Energy Detector (TED). Together these instruments monitor electron fluxes from 50 eV up to 2700 keV. For a detailed description of the SEM-2 instruments, see *Evans and Greer* [2004]. The SEM-2 package is a significant upgrade on the SEM-1 package [*Hill et al.*, 1985], which operated onboard the NOAA Television and InfraRed Observation Satellite (TIROS) spacecraft from 1978 to 2004. We make use of SEM-2 observations from up to four POES spacecraft, from the earliest date of data availability up to 20 July 2008. The starting dates are 1 July 1998 for NOAA-15, 10 January 2001 for NOAA-16, 12 July 2002 for NOAA-17, and 7 June 2005 for NOAA-18. All POES data are available from http://poes.ngdc.noaa.gov/data/; whereas the full-resolution data has 2 s time resolution, we work with the 16 s resolution ASCII files. Table 1 lists the SEM-2 detectors used in the current study, where "e" refers to electron detectors and "P" proton detectors. The 0°-pointing detectors are mounted on the three-axis stabilized POES spacecraft so that the center of each detector field of view is outward along the local zenith, parallel to the Earth-center-to-satellite radial vector. Another set of telescopes, termed the 90° detectors, are mounted approximately perpendicular to the 0° detector. In addition, there is also a set of omnidirectional measurements made from a dome detector that is mounted parallel to the 0° telescopes. The telescopes pointing in the

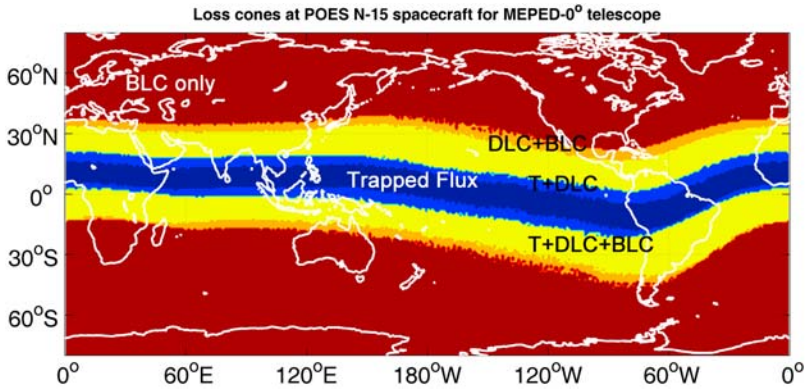

Figure 1. World map showing the changing radiation belt population observed by the 0° directed ±15° wide MEPED-telescopes onboard POES. Here T indicates trapped flux, DLC is drift-loss cone, and BLC is bounce loss cone. For the highest latitudes the instrument only measures fluxes inside the bounce-loss cone, while at lower latitudes it observes a mix of populations.

0° and 90° directions are ±15° wide, while the omnidirectional dome detectors (labeled "omni") are ±60° wide.

[8] POES user information suggests that the 0° telescopes monitor particles in the atmospheric loss cone that will enter the Earth's atmosphere below the satellite when the spacecraft is poleward of about 35°, while at high latitudes the 90° telescopes monitor particles which are trapped in the Van Allan radiation belts. Some confirmation of this comes from *Gamble et al*. [2008, Figure 5], which shows that the 90° electron telescopes include the drift-loss cone at latitudes of 30° to 40° south. The POES SEM-2 data files includes the IGRF-determined pitch angles of the particles detected by the 0° and 90° telescopes at the spacecraft. Using the IGRF magnetic model for the altitude of the NOAA-15 spacecraft in mid-2005, we have determined the angular width of the bounce and drift loss cones at the satellite, and hence the geographical variation of the particle populations was detected. Figure 1 presents a world map of the changing radiation belt population observed by the 0°-directed ±15°-wide MEPED telescopes onboard NOAA-15. This plot is representative for all four POES spacecraft included in our study and over the entire time period. In Figure 1, "T" indicates trapped flux, "DLC" is drift-loss cone, and "BLC" is bounce-loss cone. For the highest latitudes the instrument only measures fluxes inside the bounce-loss cone, i.e., precipitating beneath the spacecraft, while at lower latitudes it observes a mix of populations. This limit, above which the 0° telescope views only the BLC, corresponds approximately to $L > 1.4$. Note that at very high latitudes, while the 0° telescopes will only be observing particles inside the BLC, they will not view the entire BLC and hence may not provide a fully accurate measure of BLC fluxes. As an example of the pitch angle range examined by this telescope, consider the point 34.5°E, 61.5°N ($L = 3.9$). At this location, the center of the 0°-directed MEPED telescopes are measuring electrons with pitch angles of 20.8°, while the edge of the BLC angle at the satellite is 58.4°, and the edge of the DLC is 59.6°. Clearly the upper and lower edges of the ±15°-wide telescopes are viewing only BLC fluxes at this location, as the upper (35.8°) and lower edges (5.8°) of the telescope's viewing range is entirely inside the BLC. When mapped to the geomagnetic equator, the center of the 0° directed MEPED telescopes measure electrons with pitch angles of 2.3° and are measuring over the pitch angle range from the upper edge of 2.7° to the lower edge of 0.5°, whereas the edge of the BLC angle is 5.6°.

[9] Owing to the large angular width of the omnidirectional dome detectors the 'omni' channels include a mix of the trapped, drift-loss cone and bounce-loss cone populations for essentially all locations. *Sandanger et al.* [2007] used observations from the SEM-1 instrument package onboard NOAA-12 and argued that at high latitudes the dome instrument could be used as precipitation monitor. Our calculations, undertaken for the SEM-2 package through the same process as for the 0° telescopes outlined above, show that the ±60° wide dome detectors will detect only trapped populations at locations that are essentially on the geomagnetic equator, but elsewhere will include contributions from the T, DLC, and BLC populations up to $L \sim 15$ where the field lines become open and the IGRF-calculations fail to produce meaningful results. For the specific $L = 3.9$ location described above, the upper edge of the dome instrument would sample pitch angles of 80.8° at the satellites, which correspond to electrons with pitch angles at the geomagnetic equator of 6.5°. Thus while the dome instrument includes a mix of trapped and loss-cone populations, the low altitude of the satellite (~800–850 km) means that the trapped populations have pitch angles only slightly above the outer edge of the loss cone. This will be true for a wide range of L shells, meaning that while the fluxes from the dome detectors will not represent true loss-cone fluxes, it may indeed provide an indication of processes driving particles toward the loss cone. Note that the low altitude of the POES satellites requires that when the 0° pointing telescopes measures trapped particles, these will have equatorial pitch angles that are only slightly above the outer edge of the loss cone at the geomagnetic equator.

3. Use of "Medium"-Energy Electron Measurements

[10] In this study the SEM-2 particle observations have been combined to produce mean particle counts varying with L and time, using 0.25-L and 3 h time resolution.

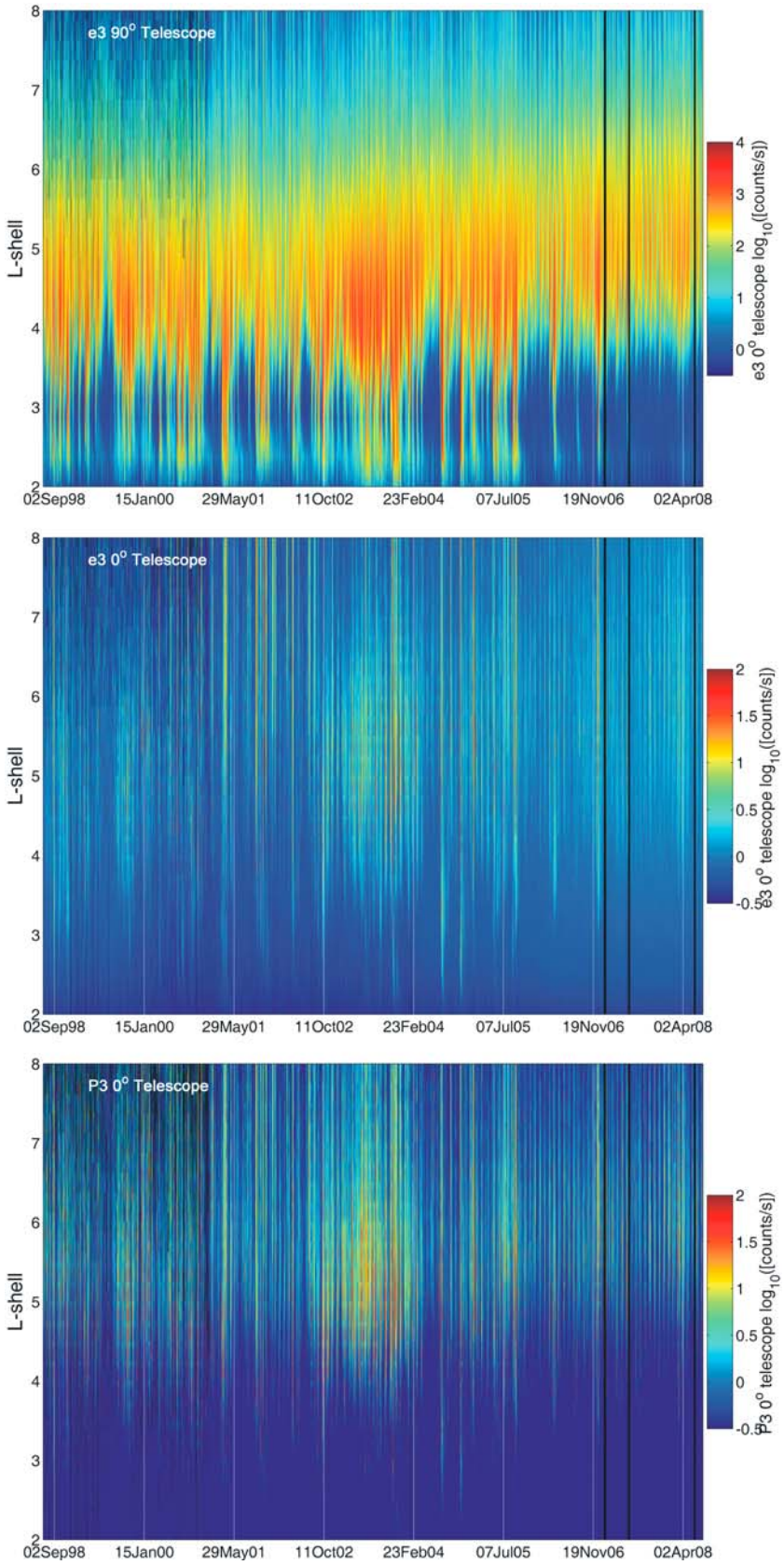

Figure 2. Variation with *L* and time of the observations from the >300 keV 90° and 0° pointing e3 "electron" telescopes and the 240 to 800 keV P3 0° proton telescope. Note the strong similarity between Figure 2 (middle) and Figure 2 (bottom).

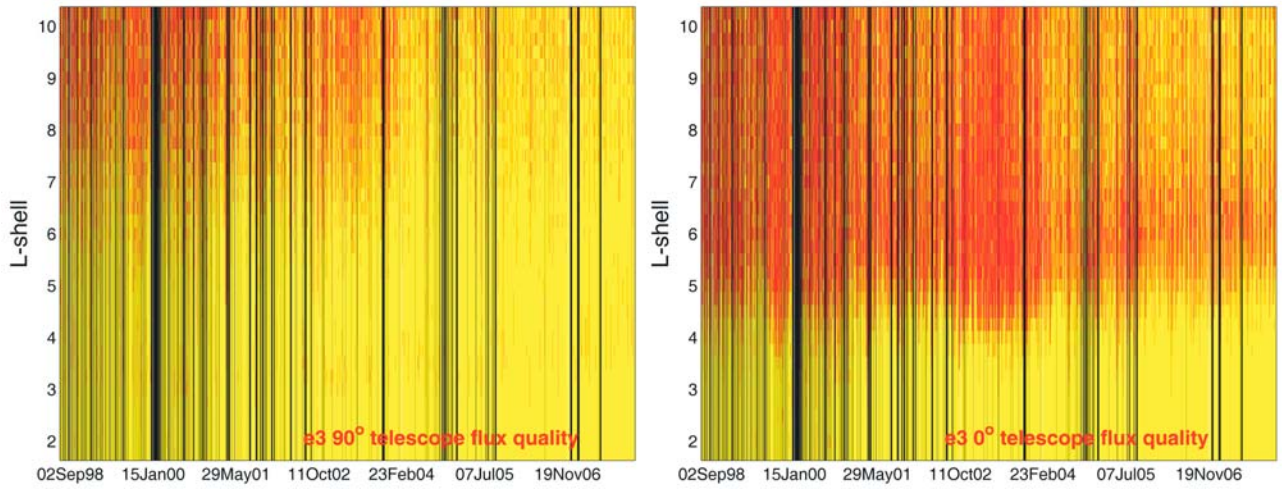

Figure 3. Variation with L and time in the data quality of the right (>300 keV 0°) and left (90°) pointing e3 "electron" telescopes. The red sections indicate where proton contamination is likely to be significant, while yellow indicates "good" quality electron counts.

Observations from inside the South Atlantic Magnetic Anomaly are excluded before the measurements are combined. Figure 2 (top) shows the variation with L and time of the counts per second reported by the e3 0° and 90° pointing telescopes, which nominally measure >300 keV electrons, while Figure 2 (bottom) shows the same data from the 240–800 keV P3 0° proton telescope. This plot spans the entire period considered from 1 July 1998 to 20 July 2008; black strips early in the plot are due to a lack of spacecraft coverage, as well as occasional data gaps that are present in 2007.

[11] Figure 2 (top) shows observations from the e3 90° telescope (trapped electrons) behaving largely as expected, with the inner and outer radiation belts visible, and occasional short-lived injections occurring through the slot-region during intense geomagnetic storms. In addition, there appears to be an overall outer radiation belt flux increase during the declining phase of the solar cycle from late 2002 to mid-2004, which is consistent with the variation of geomagnetic activity indices such as *Ap* during the recent 11-year solar cycle.

[12] As noted in the final column of Table 1, the SEM-2 e1, e2, and e3 telescopes suffer from contamination by rather low-energy protons, with one proton in the correct energy range leading to one count in the electron detector. The detector energy ranges given in Table 1 have been taken from Table 3.3.2 of *Evans and Greer* [2004], and were experimentally determined. In Figure 2 (bottom) there is a strong agreement between the variation and magnitude of the counts from the e3 and P3 0° detectors, which is suggestive of a significant contamination issue in this data set. This is also indicated by the otherwise surprisingly large L-range of >300 keV precipitation suggested by the e3 0° telescope, with large values extending to $L = 8$, well beyond the extent of the outer of the outer radiation belt as observed by the e3 90° telescope (trapped electron fluxes). In order to quantify the level of contamination in the e1, e2, and e3 telescopes, and estimate where the counts from the "electron" telescopes are most likely to be dominated by electrons, we require that the counts reported by the electron telescope be at least twice as large as the counts from the "contaminating" proton telescope because one "contaminating" proton will produce one incorrect electron count. Under these conditions, we take the electron observations to be "good" when the following hold:

$$e1 > 2 \times P2 \tag{1}$$

$$e2 > 2 \times P3 \tag{2}$$

$$e3 > 2 \times P3 \tag{3}$$

[13] Figure 3 shows the application of these conditions to the e3 telescope data, which has the most contamination from the e1, e2, and e3 detector set. Figure 3 (left) shows the contamination plot for the e3 90° detector, while Figure 3 (right) presents the e3 0° pointing telescope. Red sections indicate where proton contamination is likely to be significant, while yellow indicates "good" quality electron counts. Black sections are due to solar proton events (suppressed in our plot) or data gaps. Clearly, the trapped electron observations reported by the e3 90° detector suffer from significantly less contamination than the e3 0° detector. This is due to lower levels of trapped protons in this energy range when compared to equivalent protons in the BLC, as seen in the SEM-2 proton telescope observations. For the purposes of radiation belt studies, the 90°-pointing (trapped flux, $L > 1.4$) e1, e2, and e3 observations are of good quality, with most of the contamination occurring beyond $L = 7$, which is in the very outer part of the outer radiation belt. However, the 0°-pointing (BLC flux) e1, e2, and e3 observations have significant levels of contamination in the "heart of the radiation belts" ($L = 4.5$–5.5), with a very significant fraction of the measurements corrupted by proton contamination.

[14] Table 2 indicates the percentage of suspect observations across the L-shell range four to seven, with 3 h, 0.25-L resolution across the time range 1 December 1998 to 31

Table 2. Data Quality for the Energetic Electron Channels of the SEM-2 Package From 1 December 1998 to 31 December 2007[a]

Data Channel	Directionality	All	Quiet (AE $\leq$ 150 nT)	Disturbed (AE > 150 nT)
e1 (>30 keV)	90° (trapped)	1.3%	0.5%	2.0%
e2 (>100 keV)	90° (trapped)	0.4%	0.3%	0.6%
e3 (>300 keV)	90° (trapped)	3.5%	0.7%	6.4%
e1 (>30 keV)	0° (BLC)	22.7%	24.7%	20.6%
e2 (>100 keV)	0° (BLC)	10.2%	8.91%	11.6%
e3 (>300 keV)	0° (BLC)	41.7%	29.1%	55.0%

[a]The percentage indicates the quantity of observations potentially contaminated by protons, for the L-shell range 4 to 7, and 3 h, 0.25-L resolution.

December 2007. The time range is limited by the availability of geomagnetic auroral electrojet (AE) index from the WDC for Geomagnetism (http://wdc.kugi.kyoto-u.ac.jp/). During disturbed geomagnetic conditions (AE $\leq$ 150 nT; following *Meredith et al.* [2006]), more than 93% of the 90°-telescope observations are good quality, with the primary contamination coming from the e3 detector. On average, only 3.5% of the data from this telescope suffers from contamination. The situation is considerably more serious for the 0°-telescope observations necessary for describing energetic electron precipitation. Overall contamination is present 42% of the time for the e3 0° telescope and can reach as much as 55% during geomagnetically disturbed periods. Even in quiet periods nearly 30% of the >300 keV precipitation measurements are potentially contaminated.

[15] The large levels of proton contamination present in the SEM-2 energetic electron precipitation observations may affect the quality of geomagnetically dependant precipitation climatologies that have been developed from this data set [e.g., *Wüest et al.*, 2005]. It is not clear from the reports published that observations dominated by proton contamination have been removed before the climatology was developed. The >30, >100, and >300 keV electron telescopes in the earlier SEM-1 package onboard the NOAA TIROS spacecraft (1978–2004) also suffered from proton contamination, although for differing energies (>135 keV [*Hill et al.*, 1985]) due to the different instrument design. Precipitation climatologies developed using these data [e.g., *Codrescu et al.*, 1997] may also contain significant proton precipitation masquerading as electron events. New processing techniques are being developed to remove the proton contamination from the POES SEM-2 electron observations, rather than simply testing of contamination and excluding that data as we have undertaken in a fundamentally conservative approach. The reprocessed observations should allow new and accurate climatologies to be produced. These techniques will be detailed in a future study.

4. SEM-2 Observations of Relativistic Electrons

[16] As outlined in Table 1, SEM-2 proton detectors also suffer from contamination, falsely responding to electrons with relativistic energies [*Evans et al.*, 2008]. The P6 omnidirectional dome detector, intended to measure protons with energies >16 MeV, also responds to electrons with energies >800 keV [*Sandanger et al.*, 2007]. The detection efficiency of the P6 dome has a value of ~0.5 for an incident electron of energy ~1.5 MeV and reaches 1 for incident electrons with energy >2 MeV. As such while the $P6_{omni}$ detector responds to electrons >800 keV, it is not strictly a >800 keV electron detector due to the varying detection efficiency. While the relativistic electron observations from the omnidirectional P6 dome detector may serve to complement those from other spacecraft with relativistic electrons (e.g., SAMPEX), it is not well suited to understanding relativistic electron precipitation (REP) because it responds to a mix of trapped- and loss-cone particles. However, the P6 telescope detectors, which are designed to measure >6.9 MeV protons, also respond to either trapped or BLC electrons (depending on *L*-shell), with energies starting from 700 keV [*Millan et al.*, 2008; R. Millan, personal communication, 2008]. While the detection efficiency profile is not sharp, the two near-orthogonal P6 telescopes provide simultaneous in situ observations of both trapped and precipitating relativistic electrons ~700 keV, complicating the information on the energy of the electrons included in the counts. Given that the SEM-2 observations start from mid-1998, it may be possible in the future to produce an estimated precipitation climatology using this data set combined with some additional information on the energy spectra of the precipitating particles.

[17] Figure 4 shows the variation with *L* and time of the relativistic electrons at low altitudes reported by P6 90° detector. While these electrons are trapped, as they are observed by the low-altitude POES instruments they have pitch angles that are relatively close to the atmospheric loss cone and as such represent the population of relativistic electrons that are most easily available to pitch angle scatter into the atmosphere. The "primary" data product from the P6 telescope, >6.9 MeV protons during solar proton events (SPE), have been removed by using solar proton activity indications from the P7 omnidirectional detector, thus leaving only the relativistic electron counts. Superimposed on Figure 4 is the daily sunspot number (white line), and ICME events classified by the ACE spacecraft (red crosses). The pattern of relativistic electron counts in the P6 90° detector resembles the variability in the e3 90° detector (Figure 2, top), with a strong enhancement during the declining solar phase, but with observations primarily in the outer radiation belt. It is clear from Figure 4 that SPE do not obscure the P6 90° relativistic electron counts over significant time periods, suggesting that the SEM-2 observations may serve as a useful database of relativistic electron observations when solar proton levels are not significant.

[18] We have attempted to contrast the "size" of the enhancements described above, and particularly the P6-detected relativistic electrons, which will penetrate most deeply into the atmosphere. The behavior of the T and BLC fluxes shows several characteristic features across the ~10 years of SEM-2 relativistic electron observations. In general, there is a strong agreement in the variability of the trapped and BLC relativistic electrons. While it appears that the sensitivity of the P6 0° detector (BLC electrons) is low, such that only rather enhanced relativistic electron precipitation periods appear in the record, there is strong agreement between the near-perpendicular telescopes (not shown). A number of relativistic electron enhancements occur in both the T and BLC fluxes that repeat in a periodic (~27 day)

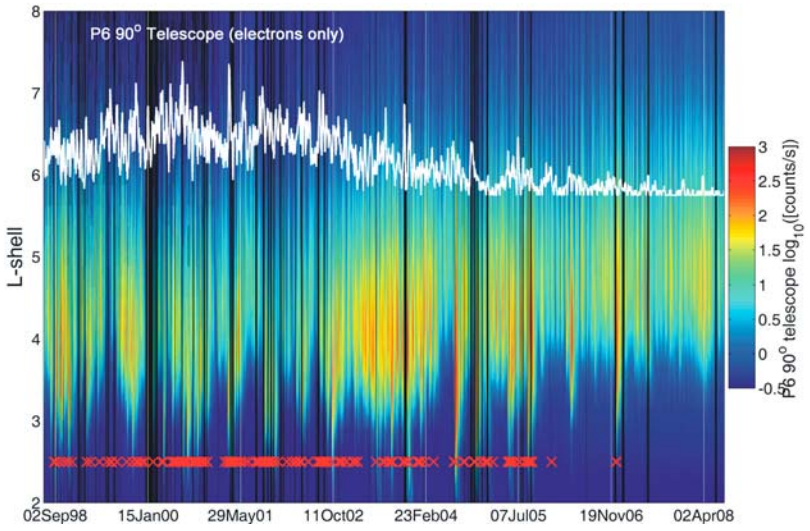

Figure 4. Variation with L and time of the relativistic electrons reported by the P6 90° detector, which responds to energetic electrons as a contamination product. Solar proton events have been removed to show the relativistic electron response. The white line is the daily sunspot number, while the red crosses mark ACE-reported ICME events.

way, apparently associated with periodic solar-wind changes. Periodic solar-wind changes associated with relativistic radiation belt-flux enhancements have been previously reported from geostationary spacecraft [*Blake et al.*, 1997]. The POES SEM-2 measurements indicate these enhancements tend to extend over approximately L = 4–7; that is, spanning the normal range of the outer radiation belt. Occasionally, enhancements in the relativistic electron populations occur that extend inward in L to L = 2–2.5. These large and deep enhancements are rare, even over the approximately 10-year data set, and tend to involve a combination of high solar-wind speeds, a large geomagnetic storm, and the arrival of an ICME. As these factors tend to occur together, it is very difficult to determine if any one factor is dominant, although it is clear that most ACE-reported transient ICMEs do not always produce such deep enhancements.

[19] Because it was not designed to measure relativistic electrons, the P6 0° detector often reports fluxes near the noise floor of the instrument, and only reports substantial relativistic electron precipitation fluxes during somewhat more intense events. This is less of an issue with the P6 90° detector, which is measuring trapped relativistic electron fluxes, at least outside of SPE times. It may be possible to enhance the dynamic range of the SEM-2 precipitating relativistic electron observations by noting that during periods when the P6 0° detector is responding to REP there is a near-constant ratio between the P6 90° and P6 0° detectors, as shown in Figure 5 for 2006. The same ratio is seen in the other years (mid-1998 onward). As before, SPE periods have been removed from the data, leading to black strips. The ACE reported solar wind speed (white line), ACE determined-ICME events (red crosses), and D_{st} variation (yellow line) have been added for context. When the P6 0° detector reports REP, the trapped flux in the P6 90° detector is about 50–70 times higher. Figure 5 (bottom) shows the variation of the one-day average of this ratio for L = 5. Once the response of the P6 instrument to relativistic electrons has been fully explored (following the work reported by *Millan et al.* [2008]) it should be possible to use the P6 90° observations as a proxy for REP. We note that the physics behind this relationship is in itself interesting because it suggests a strong coupling (on average) between the trapped and precipitating fluxes, at least on 3 h timescales and at the low-Earth orbit altitudes in which the POES spacecraft are located. This deserves further investigation. We suggest that Figure 5 indicates periods where ground-based data might be examined for precipitation events.

5. Relativistic Electron Enhancements at Low Altitudes and Near the Geomagnetic Equator

[20] Following on from section 4, we have undertaken a more detailed examination of SEM-2 observations during the periodic enhancements in trapped-electron fluxes, which are likely driven by high-speed solar wind-streams, and contrasted these with GOES measurements made near the geomagnetic equator. We particularly focus on the periodic enhancements because these are well suited to check for energy-dependent time delays. Such periods have been identified using ACE-reported solar-wind speed, as listed in Table 3. Figure 6 (top left) shows the time variation in the mean electron counts inside a statistically determined plasmapause model [*Moldwin et al.*, 2002] from the e3 90° and P6 90° telescopes over the period 1 July to 31 December 2007. In this case, we limit ourselves to counts from L = 2.5 to the plasmapause. Observations from the detectors, at times which are likely to be affected by proton contamination, have been suppressed from the plot, using the criteria outlined in section 3. The plot shows one-day average values, which have each been normalized to the maximum daily mean-count rate observed during this period so that they appear clearly on this plot. From mid-August 2007 there are a series of periodic geomagnetic disturbances, as shown by the variation in Kp (black line), which has been normalized in the same manner as the electron counts. The periodic geomagnetic disturbances are most likely driven by the periodic

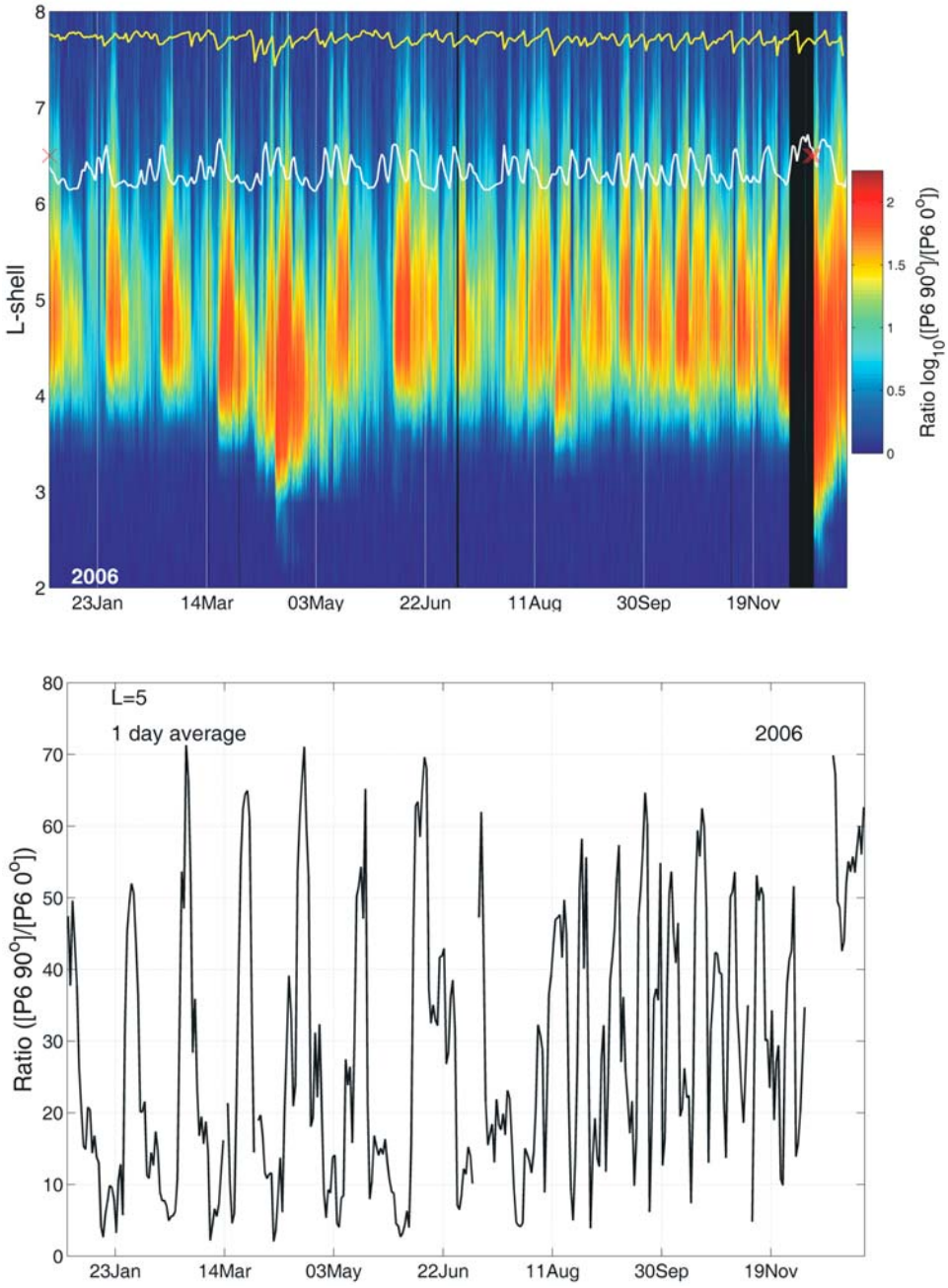

Figure 5. The ratio between the relativistic electron counts (electrons above 700 keV) reported by the P6 90° and P6 0° detectors during 2006. The ACE reported solar wind speed (white line), ACE determined-CME events (red crosses), and D_{st} variation (yellow line) are also shown in Figure 5 (top). Figure 5 (bottom) is a line plot for $L = 5$, showing the variation of this ratio with a one-day average.

changes in solar-wind speed (red dash-dotted line). Figure 6 (lower left) has had an energy-dependant time delay applied to the counts reported by each detector, as described in the legend. This causes the electron enhancements to line up with the geomagnetic disturbance variability quite cleanly, suggesting that the enhancement mechanism progressively raises the energy of electrons through the three "medium" electron detectors upward toward the relativistic electron observations. We have examined the time shifts appropriate for the e1, e2, and e3 90° telescopes, the P6 90° telescope, and the P6 omnidirectional dome detector over this period. These data are displayed in Table 3. While the >30 keV electron enhancement occurs about one day after the geomagnetic driver (much like the timescales already reported at the geomagnetic equator), the relativistic electron enhancement measured by the omnidirectional P6 dome detector is delayed ~12 days from the driver.

[21] Figure 6 (top right) shows the nonshifted and time-delayed (bottom right) variation in the mean electron counts outside a statistically determined plasmapause; in this case

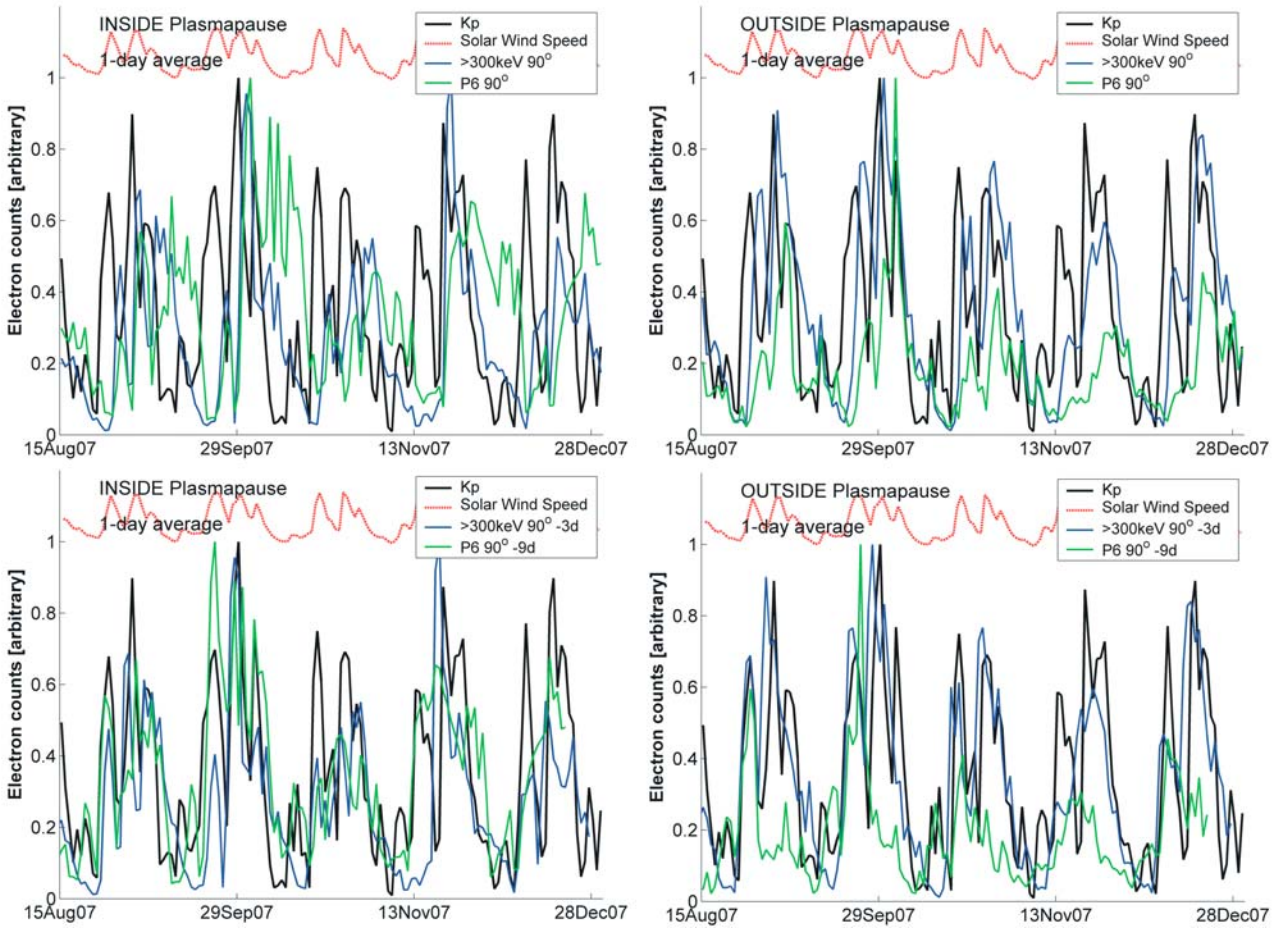

Figure 6. Time variation in the mean normalized electron counts inside and outside a statistically determined plasmapause from the e3 90° and P6 90° telescopes for the period 15 August to 31 December 2007. The variation in Kp (black line) and solar wind speed (red dash-dotted line) are shown for context. Figure 6 (bottom) shows the same count information as Figure 6 (top), but with an energy-dependent delay applied.

from the plasmapause out to $L = 7$. The range of the inner ($L = 2.5$) and outer ($L = 7$) limits come from the observations discussed in section 4. While the variability in the POES-observed electron counts is different outside the plasmapause than inside, in this case the same set of energy-dependent delays (Table 3) does an equally adequate job of linking the enhancements to the geomagnetic driver. The fact that the line structure in the P6 90° telescope is quite different inside the plasmapause compared with outside the plasmapause suggests significant differences in the processes of acceleration, transport, and loss either side of the plasmapause in response to this HSSWS driver.

[22] Many of the acceleration processes that produce enhancements in the trapped energetic electron fluxes work preferentially on electrons with low pitch angles (e.g., <30° [*Horne et al.*, 2005]); thus, one might expect a time delay before a significant population of relativistic electrons arrives at the altitudes of low-Earth orbiting satellites or begin precipitating into the atmosphere. However, this is not borne out by a comparison of the time delays seen in the low-altitude POES observations with electron flux measurements from instruments onboard GOES-12 located near the geomagnetic equator. Figure 7 shows the daily average fluxes of GOES-observed electrons with energies >0.6 MeV (magenta line) and >2 MeV (cyan line), plotted with the beyond-the-plasmapause POES-observations from Figure 6. In Figure 7 (top) the same format is used to present observations with no time delay. Figure 7 (bottom) includes an energy-dependent time delay. Generally, the time variation of the >600 keV electron fluxes at geostationary altitudes, and thus near the geomagnetic equator, is very similar to those of the >300 keV electron fluxes at low altitudes, and thus near the atmospheric loss cone. The same is true of the GOES >2 MeV electron fluxes and the POES P6 90° telescopes. Note that the two GOES energy channels do not cleanly track one another, which is consistent with the behavior shown by the POES measurements. Figure 7 (bottom) shows the GOES and POES observations subject to time offsets. As with the POES data, the GOES measurements show an energy-dependent time offset between geomagnetic activity and radiation belt electron fluxes. The delays are seen to be similar at the $L = 6.6$ geomagnetic equator when compared with fluxes measured just above the atmosphere.

Table 3. Energy-Dependent Time Delays in Days Between Geomagnetic Disturbances and POES SEM-2 Observed Increases in Energetic Electron Fluxes Inside and Outside a Statistical Model of the Plasmapause[a]

Time Period	Inside Plasmapause					Outside Plasmapause				
	>30 keV	>100 keV	>300 keV	P6 90°	$P6_{omni}$	>30 keV	>100 keV	>300 keV	P6 90°	$P6_{omni}$
Mid-August to late October 1999	1	2	3	4	5	0	1	1	2	3
Mid-August 2003 to mid-March 2004	1	1	2	5	6	1	1	2	3	4
April 2006	0	1	1	3	3	0	0	1	2	5
Mid-March to late May 2007	0	1	2	5	8	0	1	1	3	6
Mid-August to end-December 2007	1	2	3	9	12	1	2	3	9	12
Average delay in days	1	1	2	5	7	0	1	2	4	6

[a]Energy-dependent.

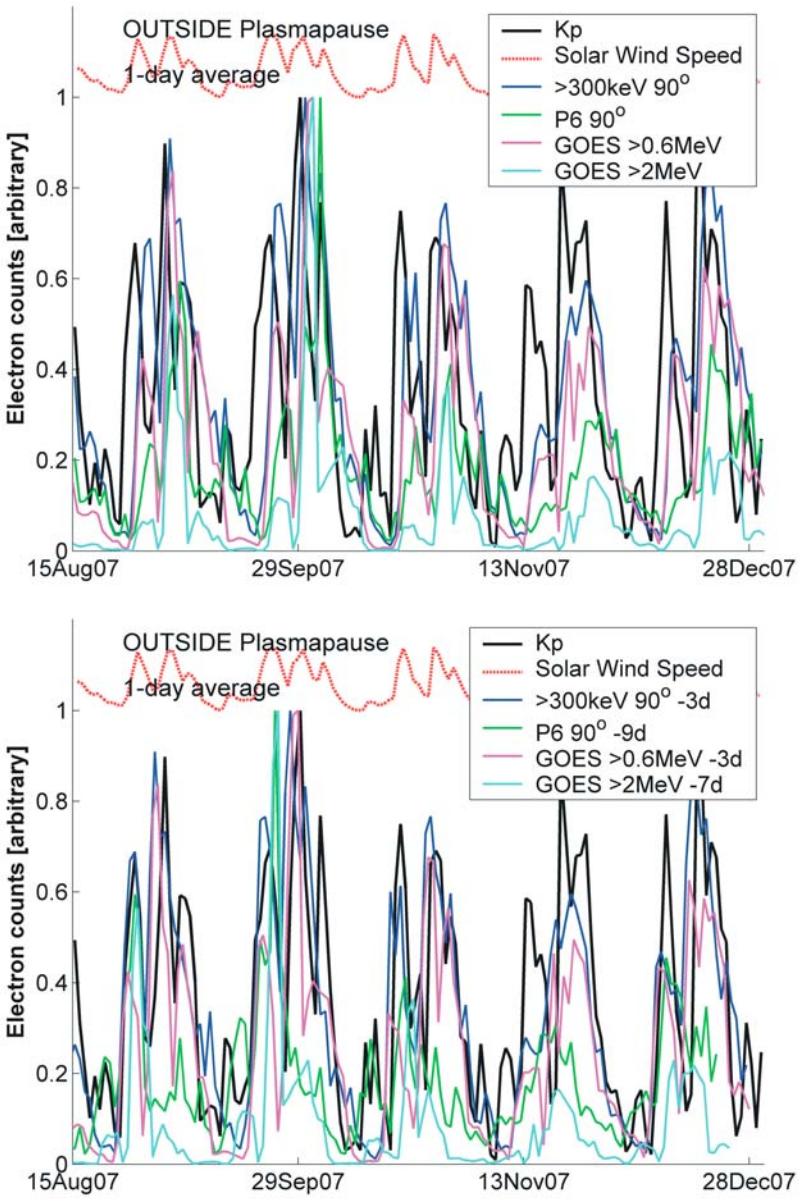

Figure 7. Time variation in the mean normalized electron counts outside a statistically determined plasmapause in the same format and time period as Figure 6. The magenta and cyan lines show the electron flux measurements from instruments onboard GOES-12, near the geomagnetic equator.

Table 4. Energy-Dependent Time Delays in Days Between Geomagnetic Disturbances and Electron Flux Measurements From Instruments Onboard GOES-12, Located Near the Geomagnetic Equator[a]

Time Period	>600 keV	>2 MeV
Mid-August to late October 1999	1	2
Mid-August 2003 to mid-March 2004	2	3
April 2006	2	3
Mid-March to late May 2007	2	5
Mid-August to end-December 2007	3	7
Average delay in days	2	4

[a]Energy-dependent.

[23] We have observed a number of similar time-delayed enhancements in the POES SEM-2 data with varying levels of time delay (Table 3). The contrasting GOES time delays for the same time periods are described in Table 4. In all cases there is a similar time delay between the geomagnetic driver and the POES >−300 keV and GOES >600 keV measurements, and the geomagnetic driver and the POES P6 90° telescope and GOES >2 MeV measurements. While the late 2007 period shows the most extreme and clear example of time-delayed relativistic electron enhancements both inside and outside the plasmapause, on average there is a six-day interval between the occurrence of the >30 keV electron enhancement and the $P6_{omni}$ relativistic electron enhancement (Table 3). In some cases we find that the energy-dependent offsets are slightly different for inside and outside the plasmapause, suggesting that the large variations in cold plasma density, which produce quite large differences in wave activity may influence the pitch-angle diffusion of the enhancements from near to the geomagnetic equator toward the atmosphere. The time delay is often slightly smaller outside the plasmapause than inside, but this effect is somewhat subtle. This may be due to the significant uncertainties (with standard deviations up to ±1 *L*-shell) reported from the plasmasphere model [*Moldwin et al.*, 2002].

[24] All the analysis outlined above was initially undertaken "by eye" looking for the best fit between the plotted geomagnetic variation and electron flux observations. However, we have also confirmed the scale sizes of the energy-dependent time delays given in Tables 3 and 4 using cross-correlation analysis. The cross-correlation analysis sometimes becomes unreliable in the case of occasional gaps in the data sequences. In addition, at the highest energy channels the delays present can be long enough relative to the fundamental recurrent activity period to confuse the analysis technique, giving negative correlation delays for the highest energy channels. We therefore provide the time delays in Tables 3 and 4, noting that they are reasonably consistent both with a formal cross correlation to determine the time lags and with "by eye" analysis.

[25] *Shprits et al.* [2009] and *Shprits* [2009] examined the processes required to transfer the relatively rapid acceleration that initially takes place near the geomagnetic equator and might be produced by chorus waves [*Horne et al.*, 2005] into precipitating electrons. These studies found that other wave processes (e.g., magnetosonic waves and EMIC waves) are required to pitch-angle scatter the near-equatorial enhancements toward the atmosphere loss cone. The GOES and POES measurements indicate that these scattering processes are comparatively rapid, such that the enhancements spread along the entire field line (i.e., spread in pitch-angle space) on a similar time scale as the acceleration process itself, so that there is a similar time variation in the electron fluxes at the geomagnetic equator and near the atmospheric loss cone. The presence of time delays is consistent with a "cartoon" view of electron acceleration processes, for example through cyclotron interactions with VLF waves [*Horne et al.*, 2005] such that electrons are accelerated to progressively higher energies over time.

[26] The link between the geostationary and low-altitude electron flux variation emphasizes the importance of multiple wave processes necessary to accelerate and pitch-angle scatter energetic electrons, coupling changes in solar output to the atmosphere. During typical "ambient" conditions, different wave activities are concentrated into different magnetic local time (MLT) regions [*Summers et al.*, 1998; *Shprits et al.*, 2008], and acceleration from processes such as chorus would be concentrated into one MLT region, whereas the wave activity driving the electron enhancements across a wide range of pitch angles will occur in different MLT regions. However, the energetic electrons in question drift rapidly around the Earth, and thus can be expected to sample all wave types in a short time period. In addition, during periods of enhanced geomagnetic activities the "normal" picture of wave activity with MLT can change, as has been reported for equatorial chorus waves that spread from the morning sector into the nightside [*Meredith et al.*, 2003].

[27] While the POES spacecraft are in Sun-synchronous orbits that sample small ranges of MLT, the inclusion of observations from multiple satellites allows a consideration of MLT dependence. From 2003 onward, there were three NOAA POES spacecraft operating with SEM-2 instrument packages, and four from mid-2005 onward. However, the time delays and enhancements seen in the 90° telescopes considered here do not show significant MLT dependence. We have also undertaken tests using a fixed *L*-shell range, rather than making use of the statistical plasmapause model, particularly focused upon the range of L = 4.5–5.5, the "heart of the radiation belts." These tests indicated the time delays were still clearly present, such that atmospheric precipitation into this *L*-shell range are likely to experience these time delays in the energy components.

[28] These results are consistent with other studies that have examined relativistic electrons at geostationary orbits. For example, *Reeves et al.* [2003] used observations from the Los Alamos National Laboratory (LANL) space environment monitors to examine the response of outer belt relativistic electrons (1.8–3.5 MeV) at geostationary orbits to 276 geomagnetic storms. They defined the defined the "post-storm flux" as the maximum flux in the one to five days after the storm. As the average time delay that we observed in the GOES >2 MeV measurements is four days, these two windows will generally overlap. The LANL space environment monitors have nine energy channels spanning 50 keV–1.5 MeV and an integral detector that responds to relativistic electrons with energies >1.5 MeV. The analysis presented in this paper could usefully be applied to the LANL data sets to better examine the energy dependence of the time offsets at geostationary altitudes (nominally $L \approx 6.6$).

For example, Figure 5 of *Longden et al.* [2008] shows a superposed epoch analysis of LANL flux data sets for both ICME and periodic HSSWS, and appears to show energy-dependent offsets in the case of HSSWS-driven storms. We acknowledge that this data set is likely to provide a very useful source for such a study, although currently significant time periods are not available for public dissemination (R. Friedel, personal communication, 2009).

[29] The energy-dependent time delays will make it more difficult to produce a representative precipitation climatology, particularly for electron energies >100 keV. For example, the *Codrescu et al*. [1997] electron precipitation climatology uses the TIROS/SEM-1 observations to extend earlier climatologies beyond 30 keV, organized through a geomagnetic "activity index," which is essentially binned Kp [*Fuller-Rowell and Evans*, 1987]. However, this will mix low-medium Kp periods before storms, when precipitating fluxes will be low, with low-medium Kp periods after storm-triggered injections, where precipitating fluxes of >100 keV electrons can be high due to delayed acceleration.

6. Summary and Conclusions

[30] Coupling between the Van Allen radiation belts and the Earth's ionosphere through precipitating particles is an area of increased scientific interest due to a growing focus on the physics of the radiation belts and also the response of the atmosphere to precipitating particles. Outstanding issues surround our understanding of the precipitation of "medium" (>20 keV) and highly energetic (relativistic) electrons, which are needed for comparison with other experimental data sets, and also to drive theoretical models. In this paper we examine roughly 10 years of measurements of trapped and precipitating electrons available from the SEM-2 instrument package onboard the POES. This data set includes both medium and relativistic energy-range measurements of trapped and precipitating electrons from the same spacecraft.

[31] Here we have shown that the POES SEM-2 detectors suffer from some contamination issues that complicate the understanding of the measurements, but that the observations provide additional insight into the precipitation of energetic electrons from the radiation belts and may be developed into a useful climatology. In particular, the 0°-directed MEPED-telescopes view only the locally precipitating fluxes in the BLC from geomagnetic latitudes corresponding approximately to $L > 1.4$.

[32] As has been known for some time, the "medium" electron energy channels in the SEM-2 instrument can suffer from contamination by rather low-energy protons. The 90°-pointing (trapped flux) >30, >100, and >300 keV electron observations are not badly affected, with most of the contamination occurring beyond $L = 7$, which is in the very outer part of the outer radiation belt. As such, these observations are well suited for the purposes of radiation belt studies. However, the 0°-pointing (BLC) electrons from these energies have significant levels of contamination in the "heart of the radiation belts" ($L = 4.5$ to 5.5) with a significant fraction of the measurements dominated by proton contamination. Contamination can reach 55% during geomagnetically disturbed periods. Even in quiet periods nearly 30% of the >300 keV precipitation measurements are potentially contaminated. The large levels of proton contamination present in the SEM-2 energetic electron precipitation observations may affect the quality of geomagnetically dependant precipitation climatologies that have been developed from this data set. It is likely that similar issues apply to the precipitation climatologies developed from the early SEM-1.

[33] The SEM-2 proton detectors also suffer from contamination, responding to electrons at relativistic energies [*Evans et al.*, 2008]. The P6 telescope detectors, which are designed to measure >6.9 MeV protons, also respond to electrons with energies from 700 keV upward [*Millan et al.*, 2008], providing simultaneous in situ observations of both trapped and precipitating relativistic electrons from mid-1998. In contrast, the P6 0° detector only reports relativistic electrons during somewhat more intense events. However, taking this into account there is very strong agreement between the behavior of the trapped and precipitating relativistic electrons, at least on 3 h timescales. Relativistic electron increases are associated with both ICME and periodic HSSWS. It is clear from our investigation that solar proton events do not obscure the trapped relativistic electron counts over significant time periods, and that the POES/SEM-2 observations may serve as a useful database of new relativistic electron observations and particularly, identifying periods of strong REP.

[34] Finally, there is an energy-dependent time delay observed in the POES/SEM-2 observations, with an almost one-week delay between the >30 keV electron enhancement and the $P6_{omni}$ relativistic electron enhancement. One possible interpretation of this is a two-stage process, where relatively rapid acceleration initially takes place near the geomagnetic equator as predicted by theory and observed experimentally. This is followed by a much slower process, where the relativistic electrons scatter toward the atmosphere loss cone at a rate that is energy dependent. Such large delays should have consequences for the timing of the atmospheric impact of HSSWS-triggered geomagnetic storms. While there appears to be some cold-plasma density dependence in the energy-dependent delay, this effect is not particularly strong, which may reflect the significant uncertainties associated with the statistical plasmasphere model we employ. In contrast, there are clearly significant differences in the variability of POES-observed electron counts inside the plasmapause when compared with outside the plasmapause, suggesting significant differences in the processes of acceleration, transport, and loss either side of the plasmapause in response to this HSSWS-driver.

[35] **Acknowledgments.** C.J.R. would like to thank the British Antarctic Survey for hosting him during his sabbatical and Kirsten Franklin of Dunedin for her support during that time. The authors wish to thank the ACE Science Center, the Kyoto World Data center, and many years' worth of efforts from NOAA personnel, who developed, maintain, and operate the NOAA/POES spacecraft.

[36] Zuyin Pu thanks Marit Sandanger, Reiner Friedel and Geoffrey Reeves for their assistance in evaluating this paper.

References

Alfonsi, L., et al. (2008), Probing the high latitude ionosphere from ground-based observations: The state of current knowledge and capabilities during IPY (2007–2009), *J. Atmos. Sol. Terr. Phys.*, *70*(18), 2293–2308, doi:10.1016/j.jastp.2008.06.013.

Blake, J. B., D. N. Baker, N. Turner, K. W. Ogilvie, and R. P. Lepping (1997), Correlation of changes in the outer-zone relativistic-electron population with upstream solar wind and magnetic field measurements, *Geophys. Res. Lett.*, *24*(8), 927–929, doi:10.1029/97GL00859.

Borovsky, J. E., and M. H. Denton (2006), Differences between CME-driven storms and CIR-driven storms, *J. Geophys. Res.*, *111*, A07S08, doi:10.1029/2005JA011447.

Brasseur, G., and S. Solomon (2005), *Aeronomy of the Middle Atmosphere*, 3rd ed., D. Reidel Dordrecht, Netherlands.

Clilverd, M. A., C. J. Rodger, and T. Ulich (2006), The importance of atmospheric precipitation in storm-time relativistic electron flux drop outs, *Geophys. Res. Lett.*, *33*, L01102, doi:10.1029/2005GL024661.

Clilverd, M. A., et al. (2009), Remote sensing space weather events: The AARDDVARK network, *Space Weather*, *7*, S04001, doi:10.1029/2008SW000412.

Codrescu, M. V., T. J. Fuller-Rowell, R. G. Roble, and D. S. Evans (1997), Medium energy particle precipitation influences on the mesosphere and lower thermosphere, *J. Geophys. Res.*, *102*(A9), 19,977–19,987, doi:10.1029/97JA01728.

Evans, D. S., and M. S. Greer (2004), *Polar Orbiting Environmental Satellite Space Environment Monitor–2 Instrument Descriptions and Archive Data Documentation*, *NOAA Tech. Mem. 1.4*, Space Environ. Lab., Boulder, Colorado.

Evans, D., H. Garrett, I. Jun, R. Evans, and J. Chow (2008), Long-term observations of the trapped high-energy proton population ($L < 4$) by the NOAA Polar Orbiting Environmental Satellites (POES), *Adv. Space Res.*, *41*(8), 1261–1268, doi:10.1016/j.asr.2007.11.028.

Friedel, R. H. W., G. D. Reeves, and T. Obara (2002), Relativistic electron dynamics in the inner magnetosphere–a review, *J. Atmos. Sol. Terr. Phys.*, *64*(2), 265–282, doi:10.1016/S1364-6826(01)00088-8.

Fuller-Rowell, T., and D. Evans (1987), Height-integrated Pedersen and Hall conductivity patterns inferred from the TIROS-NOAA satellite data, *J. Geophys. Res.*, *92*(A7), 7606–7618, doi:10.1029/JA092iA07p07606.

Gamble, R. J., C. J. Rodger, M. A. Clilverd, J. A. Sauvaud, N. R. Thomson, S. L. Stewart, R. J. McCormick, M. Parrot, and J.-J. Berthelier (2008), Radiation belt electron precipitation by manmade VLF transmissions, *J. Geophys. Res.*, *113*, A10211, doi:10.1029/2008JA013369.

Green, J. C., T. G. Onsager, T. P. O'Brien, and D. N. Baker (2004), Testing loss mechanisms capable of rapidly depleting relativistic electron flux in the Earth's outer radiation belt, *J. Geophys. Res.*, *109*, A12211, doi:10.1029/2004JA010579.

Hill, V. J., D. S. Evans, and H. H. Sauer (1985), *TIROS/NOAA Satellites Space Environment Monitor Archive Tape Documentation*, *NOAA Technical Memorandum ERL SEL-71*, Space Environ. Lab., Boulder, Colorado.

Hilmer, R. V., G. P. Ginet, and T. E. Cayton (2000), Enhancement of equatorial energetic electron fluxes near $L = 4.2$ as a result of high-speed solar wind-streams, *J. Geophys. Res.*, *105*(A10), 23,311–23,322, doi:10.1029/1999JA000380.

Horne, R. B. (2002), The contribution of wave-particle interactions to electron loss and acceleration in the Earth's radiation belts during geomagnetic storms, in *URSI Review of Radio Science 1999–2002*, edited by W. R. Stone, pp. 801–828, John Wiley, Hoboken, N. J.

Horne, R. B., R. M. Thorne, S. A. Glauert, J. M. Albert, N. P. Meredith, and R. R. Anderson (2005), Timescale for radiation belt electron acceleration by whistler mode chorus waves, *J. Geophys. Res.*, *110*, A03225, doi:10.1029/2004JA010811.

Longden, N., M. H. Denton, and F. Honary (2008), Particle precipitation during ICME-driven and CIR-driven geomagnetic storms, *J. Geophys. Res.*, *113*, A06205, doi:10.1029/2007JA012752.

Lorentzen, K., M. Looper, and J. Blake (2001), Relativistic electron microbursts during the GEM storms, *Geophys. Res. Lett.*, *28*(13), 2573–2576, doi:10.1029/2001GL012926.

Meredith, N. P., R. B. Horne, R. M. Thorne, and R. R. Anderson (2003), Favored regions for chorus-driven electron acceleration to relativistic energies in the Earth's outer radiation belt, *Geophys. Res. Lett.*, *30*(16), 1871, doi:10.1029/2003GL017698.

Meredith, N. P., R. B. Horne, M. A. Clilverd, D. Horsfall, R. M. Thorne, and R. R. Anderson (2006), Origins of plasmaspheric hiss, *J. Geophys. Res.*, *111*, A09217, doi:10.1029/2006JA011707.

Millan, R. M., K. Yando, and J. C. Green (2008), NOAA POES observations of relativistic electron precipitation during a radiation belt depletion event, *Eos Trans. AGU*, *89*(53), *Fall Meet.* Suppl., Abstract U13A–0043.

Miyoshi, Y., and R. Kataoka (2005), Ring current ions and radiation belt electrons during geomagnetic storms driven by coronal mass ejections and corotating interaction regions, *Geophys. Res. Lett.*, *32*, L21105, doi:10.1029/2005GL024590.

Moldwin, M. B., L. Downward, H. K. Rassoul, R. Amin, and R. R. Anderson (2002), A new model of the location of the plasmapause: CRRES results, *J. Geophys. Res.*, *107*(A11), 1339, doi:10.1029/2001JA009211.

Randall, C. E., et al. (2005), Stratospheric effects of energetic particle precipitation in 2003–2004, *Geophys. Res. Lett.*, *32*, L05802, doi:10.1029/2004GL022003.

Reeves, G. D., et al. (2003), Acceleration and loss of relativistic electrons during geomagnetic storms, *Geophys. Res. Lett.*, *30*(10), 1529, doi:10.1029/2002GL016513.

Reeves, G., A. Chan, and C. J. Rodger (2009), Current understanding of radiation belt dynamics and future challenges, *Space Weather*, *7*, S07004, doi:10.1029/2008SW000436.

Richardson, I. G., E. W. Cliver, and H. V. Cane (2000), Sources of geomagnetic activity over the solar cycle: Relative importance of coronal mass ejections, high-speed streams, and slow solar wind, *J. Geophys. Res.*, *105*(A8), 18,203–18,213, doi:10.1029/1999JA000400.

Rozanov, E., L. Callis, M. Schlesinger, F. Yang, N. Andronova, and V. Zubov (2005), Atmospheric response to NO_y source due to energetic electron precipitation, *Geophys. Res. Lett.*, *32*, L14811, doi:10.1029/2005GL023041.

Sandanger, M., F. Søraas, K. Aarsnes, K. Oksavik, and D. S. Evans (2007), Loss of relativistic electrons: Evidence for pitch angle scattering by electromagnetic ion cyclotron waves excited by unstable ring current protons, *J. Geophys. Res.*, *112*, A12213, doi:10.1029/2006JA012138.

Seppälä, A., M. A. Clilverd, and C. J. Rodger (2007), NO_x enhancements in the middle atmosphere during 2003–2004 polar winter: Relative significance of solar proton events and the aurora as a source, *J. Geophys. Res.*, *112*, D23303, doi:10.1029/2006JD008326.

Seppälä, A., C. E. Randall, M. A. Clilverd, E. Rozanov, and C. J. Rodger (2009), Geomagnetic activity and polar surface air temperature variability, *J. Geophys. Res.*, *114*, A10312, doi:10.1029/2008JA014029.

Shprits, Y. Y. (2009), Potential waves for pitch-angle scattering of near-equatorially mirroring energetic electrons due to the violation of the second adiabatic invariant, *Geophys. Res. Lett.*, *36*, L12106, doi:10.1029/2009GL038322.

Shprits, Y. Y., et al. (2008), Review of modeling of losses and sources of relativistic electrons in the outer radiation belt II: Local acceleration and loss, *J. Atmos. Sol. Terr. Phys.*, *70*(14), 1694–1713, doi:10.1016/j.jastp.2008.06.014.

Shprits, Y. Y., L. Chen, and R. M. Thorne (2009), Simulations of pitch angle scattering of relativistic electrons with MLT-dependent diffusion coefficients, *J. Geophys. Res.*, *114*, A03219, doi:10.1029/2008JA013695.

Summers, D., R. M. Thorne, and F. Xiao (1998), Relativistic theory of wave-particle resonant diffusion with application to electron acceleration in the magnetosphere, *J. Geophys. Res.*, *103*(A9), 20,487–20,500, doi:10.1029/98JA01740.

Turunen, E., P. T. Verronen, A. Seppälä, C. J. Rodger, M. A. Clilverd, J. Tamminen, C. F. Enell, and T. Ulich (2009), Impact of different energies of precipitating particles on NO_x generation in the middle and upper atmosphere during geomagnetic storms, *J. Atmos. Sol. Terr. Phys.*, *71*, 1176–1189, doi:10.1016/j.jastp.2008.07.005.

Ukhorskiy, A. Y., B. J. Anderson, P. C. Brandt, and N. A. Tsyganenko (2006), Storm time evolution of the outer radiation belt: Transport and losses, *J. Geophys. Res.*, *111*, A11S03, doi:10.1029/2006JA011690.

Vassiliadis, D., I. R. Mann, S. F. Fung, and X. Shao (2007), Ground Pc3-Pc5 wave power distribution and response to solar wind velocity variations, *Planet. Space Sci.*, *55*(6), 743–754, doi:10.1016/j.pss.2006.03.012.

Wüest, M., R. A. Frahm, J. K. Jennings, and J. R. Sharber (2005), Forecasting electron precipitation based on predicted geomagnetic activity, *Adv. Space Res.*, *36*(12), 2445–2450, doi:10.1016/j.asr.2003.12.014.

M. A. Clilverd and M. M. Lam, Physical Sciences Division, British Antarctic Survey, High Cross, Madingley Road, Cambridge CB3 0ET, UK.

J. C. Green, Space Environment Center, NOAA, 325 Broadway Blvd., Boulder, CO 80305, USA.

C. J. Rodger, Department of Physics, University of Otago, PO Box 56, Dunedin, New Zealand. (crodger@physics.otago.ac.nz)